SPACE DEBRIS DATABASE FOR RE-ENTRY EVENTS PREDICTION

E. Pignacca, E. Mooij, and V. Fossa

Delft University of Technology, Faculty of Aerospace Engineering, Kluyverweg 1, 2629 HS Delft, The Netherlands,
Email: e.pignacca@tudelft.nl, e.mooij@tudelft.nl

ABSTRACT

The growing number of objects in Earth's orbit has increased the risk of collisions and fragmentation events. Space Traffic Management systems need accurate orbit propagation models to be effective. At the same time, the most commonly used aerodynamic models, such as the cannonball model, fail to account for shape, orientation, and detailed material properties, which are fundamental for accurate propagation. This study introduces a database for space debris objects. A particular interest is posed on aerodynamic properties, incorporating the Stochastic Parallel Rarefied-gas Time-accurate Analyzer software for rarefied flow, the Modified Newtonian method for continuum flow, and a bridging function for transitional flow. Although the current database is limited to objects with simple shapes, the same process can be applied to more complex geometries. The database was created for a flat plate and a cylinder and applied to an orbital decay simulation. Simulations using six degrees of freedom (6 dof) were compared against simulations using three degrees of freedom (3 dof) and a cannonball model. While the 6-dof model provides the most accurate results, it is computationally expensive. The other simulations can be performed in a fraction of the time, but their accuracy must be assessed to conclude their suitability. Results show that a cannonball approach could provide better results than the 3-dof case, but only if the drag coefficient is tailored to the 6-dof simulation. However, this would entail running the 6-dof simulation first, not fully solving the computational effort issue. Furthermore, the cannonball model performs poorly when the simulation is extended to the impact point, as the average drag coefficient in the 6-dof simulation changes. Monte Carlo analyses further highlight the impact of uncertainties in orbital decay simulations, with the 3-dof simulations performing worse than the cannonball model. It is concluded that 3-dof simulations and adjusted cannonball models are generally not accurate enough to substitute the 6-dof simulation, which, however, needs to be improved in terms of computational effort. Future work will entail expanding the database to more objects, likely with more complex geometries, and performing the orbit decay analysis with more test cases and more samples, as well as expanding the analysis to the re-entry.

Keywords: space debris database, orbital decay, propagation, rarefied and continuum aerodynamics, material properties, re-entry.

1. INTRODUCTION

The last decades have seen a significant increase in the number of objects orbiting Earth. This brings a clear consequence: the risk of fatal collisions for many categories of spacecraft - operational spacecraft, launch vehicles, and spacecraft involved in orbital transfers. Space Traffic Management (STM) Systems will help coordinate mission planning to reduce the risk of collisions, thus reducing the growth of the space-debris population. However, before such a system can be successfully developed, aspects of the environment in relation to the (numerical) propagation of objects in space should be better understood.

As documented in ESA's Space Environment Report, the number of trackable objects in space has seen a major increase over the past decades: from about 8,000 in the year 2000 to about 40,000 currently [1]. This increment is, for a large part, due to the launch of the so-called megaconstellations of communication systems, which are predicted to increase to some 100,000 in 2030. It is obvious that this development will lead to a greater number of predicted conjunctions, required evasive manoeuvres, and actual collisions. Currently, the spaceflight community counts several hundreds of conjunctions, a comparable number of evasive manoeuvres, and about 12 fragmentation events per year [1], all of them with a major impact on operational missions and the use and benefits of spaceflight.

Any satellite operator should, of course, be aware of the larger space objects, but there is more to it. One could think that the large active and inactive satellites and burnt-out rocket bodies represent the largest danger for collisions, as their size and mass are large. This would lead to the immediate destruction of both objects when they are involved in a collision. But it goes further than that: the smaller pieces of debris, being the result of previous fragmentation events (either intentional or unintentional), represent an even greater danger, if only because of the sheer numbers involved. Objects between 1 and 10 cm

Proc. 9th European Conference on Space Debris, Bonn, Germany, 1–4 April 2025, published by the ESA Space Debris Office
Editors: S. Lemmens, T. Flohrer & F. Schmitz, (http://conference.sdo.esoc.esa.int, April 2025)

that are harder, not to say impossible, to track, amount to about 900,000, and yet they can create a lot of damage when colliding with a larger object. The obvious conclusion is that the detection and tracking capabilities should be further developed. Fortunately, this is an ongoing development; for instance, the Goldstone Orbital Debris Radar can track sizes as small as 5 mm up to 1000 km altitude [2].

Due to the large number of debris objects and the line-of-sight visibility constraint, measurements are not always available. It may be that there is a measurement/orbit determination once a day or even once every few days. Therefore, for near-future predictions to assess the collision probability between any two space objects, one has to rely on the propagation of the objects' state, using the latest measurements as initial state.

The orbital motion of a space object is mainly driven by the central-field gravity force, but there are many perturbations that force the object away from its idealised orbit. Most of these perturbations are well understood, e.g., the higher-order gravity terms, third-body perturbations from Moon and Sun (a.o.), solar-radiation pressure, and atmospheric drag. However, even though the physics of the latter two is well known, even taking uncertainties in the atmosphere into consideration, the resulting accelerations are very much dependent on the shape, orientation, and surface properties of the object. Space-debris orbit propagation is typically done including a so-called cannonball model, which provides a drag force only, as the attitude of the object is ignored.

For precise and longer-term orbit predictions, the aforementioned aspects should be taken into account, of course, but with certain extensions. The most notable are the attitude of the object over time and potential material degradation, as this will affect the reflective and/or aerodynamic properties. Since large parts of the orbits are well outside the denser parts of the atmosphere, the aerodynamics is driven by rarefied-flow rather than continuum flow. An internal study has confirmed that using rarefied flow solvers are indeed crucial for accurate orbit propagation [3].

Since it is a time-consuming process to establish the properties of space-debris objects, it is proposed to review potential shapes of space-debris objects and prepare a database of sorts with surface and aerodynamics properties. These shapes can be simple in nature, e.g., plates, cubes, spheres, and cylinders. For inactive satellites or the active ones that are deorbiting, more detailed analysis can be done, taking the actual configuration into account.

The layout of the paper is as follows. Section 2 starts by introducing the space environment relevant for the propagation to be accurate enough and concludes with an overview of the equations motion. In Sec. 3, the proposed space-debris database is introduced, with its main focus on the aerodynamic properties of a selected number of shapes. This database is then used in Sec. 4 to study the orbital decay of space-debris objects. Finally, Section 5 wraps up the paper with concluding remarks.

2. ENVIRONMENT

This section outlines the space environment in which the objects reside in the test cases presented in this work. The analyses shown in Section 4 are carried out on Low Earth Orbit (LEO), with altitudes below 300 km. The simulations will consider the presence of uncertainties; given the low altitudes considered, these include features related to the upper atmosphere, summarised here. Then, the reference frames employed are introduced, together with the equations of motion that describe the dynamics of the objects.

2.1. Main Sources of Uncertainty

When observing a generic debris object, one will always have to deal with uncertainties regarding both the characteristics of the object, e.g., shape, mass, material properties and its state, e.g., position, velocity, angular rate. These uncertainties arise from limitations in observational techniques and the complex interactions with the space environment [4]. Due to the low altitude considered in this work's test cases, the object's state propagation is also affected by sources of uncertainty related to the upper atmosphere. Here, aerodynamic forces and moments are not negligible, meaning that the aerodynamic models used will influence the accuracy of the propagation. An approach that has been typically employed is to represent the object's aerodynamics using a cannonball model. However, this method neglects moments and any force other than drag. Furthermore, if the cannonball drag coefficient is chosen a priori, with little to no knowledge of the object's aerodynamic properties, the value used could greatly differ from the values that would actually occur. On the contrary, using a database with properties that depend on the object's state and are updated along the propagation can increase the state prediction accuracy [3, 5].

To analyse the differences in these approaches, three different aerodynamic models will be tested: i) a simulation that includes both translational and rotational dynamics and uses a finite-body drag model, with the aerodynamic force and moment coefficients from the database; ii) a purely translational simulation using the force coefficients from the database; iii) a purely translational simulation using a cannonball drag model, with $C_D = 2.2$ according to the standard for a "typical spacecraft" [5].

The aerodynamic modelling is not the only source of uncertainty; there are other aspects, such as the atmospheric model and solar and geomagnetic activity, that should be taken into account. One of the most used atmospheric models is the NRLMSISE-00 model [6], as it is the most accurate to date, including temporal and spatial dependencies. However, even with this model, there are uncertainties in atmospheric data, such as composition, density, and temperature. This is mainly due to the scarcity of observations at certain altitudes and for extended periods of time, with resulting datasets that can differ between different missions [5, 7]. Similarly, there is still little data that allow one to accurately predict the effects of solar and geomagnetic activity, events that can greatly disrupt the orbital motion of objects at low altitudes by changing the atmospheric properties. Furthermore, it is still difficult to predict the intensity of these occurrences with a lead time of more than a few hours [8]. It is thus of primary importance to consider the uncertainties introduced by these activities and the effects that short lead times can have on STM.

In the simulations performed in this paper, the variability due to geomagnetic and solar activity is not considered, as this issue regards propagations that are performed in longer periods of time. Currently, the US76 atmospheric model is used for ease of implementation; however, this means that the uncertainties in atmospheric density will be larger than those with a more accurate model. The implementation of the NRLMSISE-00 model is left as future work.

2.2. Reference Frames and Equations of Motion

For the purpose of the space debris database and the analysis presented in this work, three main reference frames are employed. First, the inertial reference frame, $\mathcal{F}_I$, which is Earth-centred and non-rotating. Its origin is at the Earth's centre of mass (c.o.m.), with the X_I axis pointing to the vernal equinox at J2000, while Z_I points north, along the Earth's rotational axis, and Y_I completes the right-handed frame.

The other two reference frames are both non-inertial and have their origin in the object's c.o.m.: the body frame, $\mathcal{F}_B$, which is body-fixed, and the aerodynamic frame, $\mathcal{F}_A$. In the body frame, the X_B and Z_B axes lie on the object's plane of symmetry, with the former pointing in the nominal forward direction and the latter pointing downwards, while Y_B completes the right-handed frame. In the aerodynamic reference frame, the X_A axis points in the direction of the airspeed relative to the atmosphere, while Z_A points in the direction opposite to the lift force, and Y_A completes the right-handed frame.

$\mathcal{F}_B$ and $\mathcal{F}_A$ are the frames in which the force and moment coefficients present in the database are expressed. In particular, the moment coefficients are expressed in the body frame, while the force coefficients are expressed in the aerodynamic frame, with the convention that the aerodynamic forces are positive in the negative direction of the frame's axes. Furthermore, the angles used to describe the object's attitude in the database are defined starting from the transformation between these two frames. In particular, the angle of attack (α) is the angle between the projection of the relative velocity vector on the $X_A Z_A$ plane and the X_B axis, while the sideslip angle (β) is defined as the angle between the relative velocity vector and the projection of X_B on the $X_A Y_A$ plane.

As mentioned previously, the simulations performed in this work consider both translational and rotational dynamics, either separately or combined. The translational motion of an object is described by the following equations:

$$\dot{\mathbf{r}}(t) = \mathbf{v}(t) \tag{1}$$

$$\dot{\mathbf{v}} = \frac{\mathbf{F}_I(t)}{m} \tag{2}$$

where $\mathbf{r}(t)$ is the position of the object's c.o.m. in $\mathcal{F}_I$, $\mathbf{v}(t)$ is its velocity, m is the object's mass, and $\mathbf{F}_I(t)$ is the sum of the external forces expressed in $\mathcal{F}_I$. In particular, this last term includes gravity, with spherical harmonics up to degree and order of 10, aerodynamic, and third body effects of the Sun and the Moon. Two main forces have not been included: forces due to the Earth's magnetic field and Solar Radiation Pressure (SRP). The latter was ignored due to the specific test case considered: at such low altitudes, the effect of SRP is negligible, but it should be included for test cases in geostationary orbits.

The equations that represent the rotational motion of the object are expressed in $\mathcal{F}_B$ as:

$$\mathbf{I}\,\dot{\boldsymbol{\omega}}(t) = \mathbf{M}_B(t) - \boldsymbol{\omega}(t) \times \mathbf{I}\,\boldsymbol{\omega}(t) \tag{3}$$

where $\mathbf{I}$ is the object's inertia tensor, $\boldsymbol{\omega}(t)$ its angular velocity vector, and $\mathbf{M}_B(t)$ is the sum of the external moments in $\mathcal{F}_B$, with the same components as those specified for the external forces.

3. SPACE DEBRIS DATABASE

An accurate model of the aerodynamic properties of debris is crucial for predicting their trajectories and improving mitigation strategies. This study uses both numerical simulations and analytical formulations to analyse the behaviour of objects with simple geometric shapes commonly found among space debris, with the main objective of generating accurate aerodynamic models. This can be done differently between the free-molecular flow (FMF), transition, and continuum flow regimes, as outlined in the following subsections. For the purpose of this work, this section focuses on aerodynamic modelling, but the database includes other data, among which material properties are relevant, especially when including SRP in the force modelling.

Two objects with simple geometric shapes were chosen for the test cases, namely a flat plate and a cylinder. In particular, the flat plate considered has dimensions of 1 m × 1 m × 0.015 m, to represent a piece of a solar panel. The cylinder was chosen as a rough approximation of the Delta-K upper stage, with a length of 6 m and a diameter of 1.5 m [9].

3.1. Free Molecular Flow: SPARTA

The Stochastic Parallel Rarefied-gas Time-accurate Analyzer (SPARTA)[1] was used to simulate debris interactions with the upper atmospheric environment in free-molecular flow. SPARTA is an open-source software that models the behaviour of millions of particles by performing a Direct Simulation Monte Carlo (DSMC) analysis. The object of interest needs to be “watertight” to be compatible with the simulation environment. The Blender tool for 3D modelling was used to generate the objects' geometry, subsequently saved in STL ASCII files. In a SPARTA simulation, the particles go through a hierarchical Cartesian grid that overlays the simulation box; this grid is used to group particles by grid cell for purposes of performing collision and chemistry operations. The object of interest is then divided into a triangular mesh and can be embedded in the grid. The grid can be used to efficiently find particle/surface collisions. As an output, SPARTA provides the pressure and shear force components per triangle of the mesh surface, from which the aerodynamic coefficients of the object can be derived.

The objects simulated in SPARTA do not need to be the exact same size as the ones that will be propagated, as the results can be scaled to approximate the behaviour of smaller or larger objects. The scaling factor is determined by the ratios of reference surface and length between the object of interest and the one used to generate the database. For proper scaling, the ratios of dimensions of the object, e.g., length and diameter, are to be kept constant.

The simulation setup involves key parameters that define the resolution and accuracy of the SPARTA simulations. The parameter $fnum$ determines the ratio of real, physical molecules to simulation particles, and is given by:

$$fnum = \frac{nrho \cdot box\_size}{part\_cell \cdot cell\_num} \tag{4}$$

Here, *nrho* represents the number density, *box_size* defines the volume of the simulation domain, *cell_num* denotes the number of grid cells, and *part_cell* represents the number of particles per cell. The time step used in the simulation is calculated as:

$$timestep = \frac{box\_side}{v_{rel} \cdot cell\_side \cdot factor} \tag{5}$$

where v_{rel} is the relative velocity of the object being analysed, and $factor$ is the number of time steps a particle remains in a single grid cell. The number of particles per cell was set to 8, while the simulation domain side was chosen as 4.8 m for both shapes. The computational grid consisted of 50^3 cells, and $factor$ was set to 10. The number of iterations for each shape and speed ratio was empirically determined to ensure the convergence of the aerodynamic coefficients. The values used in this study were taken from [10], except for the size of the simulation box, which could be diminished due to the smaller dimensions of the objects considered.

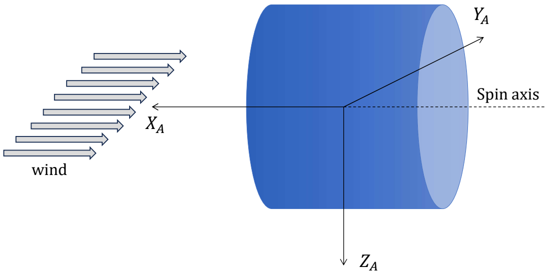

Figure 1. Cylinder reference attitude ($\alpha = \beta = 0$)

The inputs required for SPARTA are the geometry of the object, its attitude with respect to the free stream, the number density, the temperature of the gas, the wall temperature, the accommodation coefficient, the velocity of the free stream, and the air composition [11].

The attitude of the object is defined by the angles of attack and sideslip, introduced in Section 2. The reference attitude of the object also needs to be defined to understand the results. Here, it is defined as $\alpha = \beta = 0$. Figure 1 shows the reference attitude for the cylinder, defined as the one at which the relative air flow direction is parallel to the cylinder's spin axis. For the flat plate, $\alpha = \beta = 0$ occurs when the air flow direction is perpendicular to the normal of the main surface and parallel to the main sides. The angle of attack varies from $-180°$ to $+180°$, while the angle of sideslip takes values in between $-90°$ and $+90°$. The choice of grid resolution has been subject to a thorough evaluation to minimise the interpolation error while limiting the computational load. A step size of $20°$ and $5°$ was simulated for both attitude angles. The results, compared after the Piecewise Cubic Hermite Interpolating Polynomial (PCHIP) interpolation [11], showed that the $20°$ step produced errors below 2%, making it a valid choice for the simulations.

The number density is calculated as $nrho = \rho NaM$, where ρ represents the air density, Na Avogadro's number, and M the molar mass of the gas. The air composition is assumed to consist entirely of atomic oxygen, the main species at lower LEO altitudes, as this reduces the SPARTA computational effort. This assumption introduces a minimal error at higher altitudes. However, the composition could still be adjusted using the speed ratio, but this method is not implemented here [11–14]. For number densities below 10^{16}, corresponding to the FMF regime, the aerodynamic coefficients remain essentially constant. Therefore, $nrho$ has been set to this value in the present analysis.

The values of the temperature of the gas (T_∞) and the wall temperature (T_{wall}) have been kept constant at 1000 K and 400 K, respectively [11]. The accommodation coefficient is set to 1, indicating a diffusive reflection, which assumes that particles are re-emitted in all directions, following a distribution that depends on the surface temperature [12, 14]. The selection of the speed ratio was taken from [11] and the values of 1, 2, 4, 6, 10, and 14 were used for the simulations. Outside this interval, a value

---

[1] `https://sparta.github.io/doc/Manual.html`

above 14 would require very light particles, which is very unlikely to occur, while speed ratios below 1 require a correction factor [10]. The speed ratios have been used to calculate the values of the relative velocities and time step. The relative velocity between the object and the atmospheric flow relates to the speed ratio through the following [12]:

$$s = \frac{v_{rel}}{c_{mp,j}}, \quad c_{mp,j} = \sqrt{\frac{2k_B T_\infty}{m_j}} \tag{6}$$

where $c_{mp,j}$ is the most probable thermal velocity of the molecules and atoms, m_j is the mass of the considered molecular species, and k_B is the Boltzmann constant. Since the air composition has been assumed to consist entirely of atomic oxygen, $c_{mp,j}$ is set to a constant value of $1019.5\ \mathrm{ms}^{-1}$ [10].

The total number of iterations for each object had to be determined to optimise computational efficiency. While more iterations generally improve precision, they increase the computational cost. It was found that the number of iterations relates to the size of the simulation box and, consequently, to $fnum$. Decreasing the value of $fnum$ lowers the simulation runtime, with consequences for the accuracy of the results. To fix this, the number of iterations can be increased. It is possible to tune the number of iterations and $fnum$ to obtain accurate results with limited simulation runtime. Furthermore, it was found that the same $fnum$ and $timestep$ can be used for different speed ratios, with the caveat that, for lower speed ratios, more iterations are needed for accuracy.

From the SPARTA simulations, pressure and shear per surface triangle are obtained; these can be processed to derive the aerodynamic properties. The first step is to transform the pressure and shear vectors into a force vector. By summing the forces acting on each of the mesh triangles, the aerodynamic force coefficients are computed in the SPARTA aerodynamic frame ($\mathcal{F}_{A_S}$), which has the X and Z axes opposed to $\mathcal{F}_A$. To find the moment coefficients, extra steps are necessary: the force acting on each mesh triangle is transformed in $\mathcal{F}_B$ and is then multiplied by the vector distance between the centre of the mesh triangle and the c.o.m. of the object. The force and moment coefficients are calculated with [11]:

$$\begin{pmatrix} C_D \\ C_S \\ C_L \end{pmatrix}_{A_S} = \frac{1}{S_{\text{ref}}} \sum_{i=1}^{n} \Delta \mathbf{f}_i \tag{7}$$

$$\begin{pmatrix} C_l \\ C_m \\ C_n \end{pmatrix}_{B} = \frac{1}{l_{\text{ref}} S_{\text{ref}}} \sum_{i=1}^{n} \mathbf{r}_{B,i} \times \left(\mathbf{R}_{B,A_S} \cdot \Delta \mathbf{f}_i \right) \tag{8}$$

where S_{ref} and l_{ref} are the reference surface area and reference length, respectively, used to make the coefficients non-dimensional. The choice of these reference values is fundamental, as it allows to scale between objects of the same shape but different dimensions. $\Delta \mathbf{f}_i$ is the aerodynamic force acting on the single mesh element, which comprises of a pressure and shear element, $\mathbf{r}_{B,i}$ is the distance vector between the i^{th} triangle central point and the origin of $\mathcal{F}_B$, and $\mathbf{R}_{B,A_S}$ is the rotation frame to transform the force from $\mathcal{F}_{A_S}$ to $\mathcal{F}_B$. This can be found with:

$$\mathbf{R}_{B,A_S} = \begin{bmatrix} -1 & 0 & 0 \\ 0 & 1 & 0 \\ 0 & 0 & -1 \end{bmatrix} \mathbf{R}_y(\alpha) \mathbf{R}_z(-\beta) \tag{9}$$

where $\mathbf{R}_y(\alpha)$ and $\mathbf{R}_z(-\beta)$ are the standard rotation matrices around the Y and Z axis, respectively.

For the analyses presented hereafter, the aerodynamic coefficients obtained from the numerical analyses were compared with values computed using the following analytical equations, assuming diffuse reflection and FMF conditions [15]:

$$\begin{aligned} C_{p,i} = &\frac{1}{s^2} \left(\frac{2}{\sqrt{\pi}} s \sin\theta_i + \frac{1}{2} \sqrt{\frac{T_w}{T_\infty}} \right) e^{-s^2 \sin^2 \theta_i} + \\ &+ \frac{1}{s^2} \left[1 + \text{erf}(s \sin\theta_i) \right] \left[\left(\frac{1}{2} + s^2 \sin^2\theta_i \right) + \right. \\ &\left. + \frac{1}{2} \sqrt{\frac{T_w}{T_\infty}} \sqrt{\pi} s \sin\theta_i \right] \end{aligned} \tag{10}$$

$$\begin{aligned} C_{t,i} = &\frac{\cos\theta_i}{s\sqrt{\pi}} \left\{ \sqrt{\pi} s \sin\theta_i \left[1 + \text{erf}(s\sin\theta_i) \right] + \right. \\ &\left. + e^{-s^2 \sin^2 \theta_i} \right\} \end{aligned} \tag{11}$$

with $C_{p,i}$ and $C_{t,i}$ being the pressure and shear coefficients of the i^{th} panel of the object's triangular mesh, and θ_i the local inclination angle of said panel. Figure 2 shows θ_i, defined for each panel element as the angle between the relative velocity vector ($\mathbf{v}_{rel}$) and the shear unit vector ($\hat{\mathbf{t}}_i$). The normal to the panel ($\hat{\mathbf{n}}_i$) is also depicted. The dependency on the object's attitude can be inferred with [16]:

$$\sin\theta_i = -\hat{\mathbf{v}}_{rel} \cdot \hat{\mathbf{n}}_i \tag{12}$$

$$\hat{\mathbf{v}}_{rel} = -\begin{pmatrix} \cos\alpha\cos\beta & \sin\beta & \sin\alpha\cos\beta \end{pmatrix}^T \tag{13}$$

where $\hat{\mathbf{v}}_{rel}$ is the relative velocity unit vector.

Equations (10) and (11), also referred to as Sentman's equations, provide an excellent approximation of the aerodynamic coefficients when it comes to objects with simple shapes. However, when considering more complex geometries, this model does not include self-shadowing nor self-reflection. Therefore, the analytical model was used to verify the SPARTA results with simple shapes. The results of the verifications allow to formulate a protocol of sorts that should be followed when simulating objects with more complex geometries.

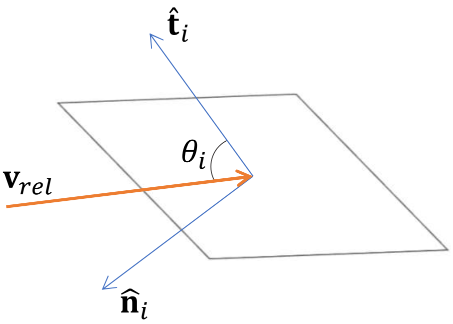

Figure 2. Local inclination of the panel element

Table 1. Comparison of C_D from SPARTA simulations for the cylinder (baseline: $C_D = 1.104$)

Iterations	Simulated C_D	Error (%)	Variation (%)
2000	0.818	35.03	N/A
2500	1.036	6.58	26.65
3000	1.084	1.91	4.63
3500	1.109	0.42	2.31
4000	1.107	0.30	0.18
5000	1.091	1.22	1.45
7000	1.112	0.68	1.92
9000	1.104	0.02	0.72

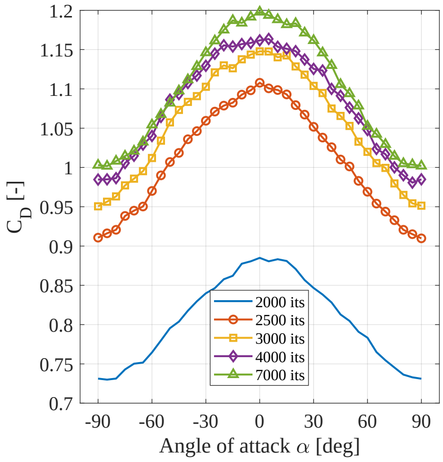

Figure 3. Cylinder variation of C_D for different numbers of iterations

Table 2. Comparison of C_D from SPARTA simulations for the flat plate (baseline: $C_D = 1.186$)

Iterations	Simulated C_D	Error (%)	Variation (%)
1500	0.891	33.03	N/A
2000	1.167	1.58	30.98
2500	1.187	0.12	1.71
3000	1.185	0.03	0.17
5000	1.184	0.16	0.08

To compare the results of these equations with the simulated values of aerodynamic coefficients, the two shapes have been evaluated at the lowest speed ratio with a varying number of iterations. The cylinder was tested over a range of 2000 to 9000 iterations, while the flat plate was tested from 1500 to 5000 iterations, as it exhibited faster convergence. This is mainly due to the different values of $fnum$ used: while the flat plate employed a value in agreement with Equation (4), the cylinder was tested with values of $fnum$ and $timestep$ that were fixed along different speed ratios to decrease the computational runtime. With simple geometries such as the flat plate and the cylinder, comparing the numerical aerodynamic force coefficients to the analytical ones is a good solution to determine the number of iterations needed. However, for objects with more complex geometries, the analytical solution might not be accurate enough. Therefore, the choice of the number of iterations must rely purely on the convergence of the results. To carry out this convergence analysis, the sideslip angle was fixed at 35° and the angle of attack ranged from $-180°$ to $+180°$ in increments of 5°. The results are shown in Tables 1 and 2, for the cylinder and the flat plate, respectively. These tables show the number of iterations used, the value of C_D at $\alpha = 40°$, the relative error between the simulated C_D and the analytical one, and the relative variation between the current simulation and the previous one, with fewer iterations. The relative variation is used to assess the convergence of the solution: if the relative variation between the current and previous simulation is small enough, the lower number of iterations is considered fit for the SPARTA simulations. For the cylinder, the analytical value of C_D is 1.104 and a minimum of 3000 iterations is required to maintain the relative variation within the chosen threshold of 3%. Note that the same conclusion could have been reached by looking at the relative error with respect to the analytical solution. At a speed ratio of 4 and beyond, 2300 iterations are sufficient to achieve this accuracy while reducing the computational time. The analytical value of C_D of the flat plate is 1.186, and the analysis showed that a minimum of 2000 runs ensures convergence with an acceptable error.

The convergence results for the cylinder and the flat plate can be visualised in Figure 3 and 4, respectively. Comparing the simulated C_D results to the baseline values, it can be observed how the convergence is not linear, but it oscillates around the analytical solution. Also, when convergence is reached, more iterations do not always imply better results due to numerical errors. An example of this can be observed in Table 1: with 4000 iterations, the simulated C_D is closer to the baseline value than with 5000 iterations. For a more detailed convergence analysis, the lift and side-force coefficient can also be studied.

The accuracy of the results obtained with SPARTA was assessed by comparing the aerodynamic coefficients from stochastic simulations with the analytical values derived from the analytical equations. Both simulated shapes

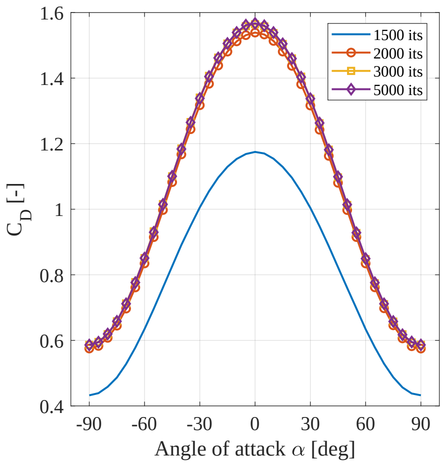

Figure 4. Flat plate variation of C_D for different numbers of iterations

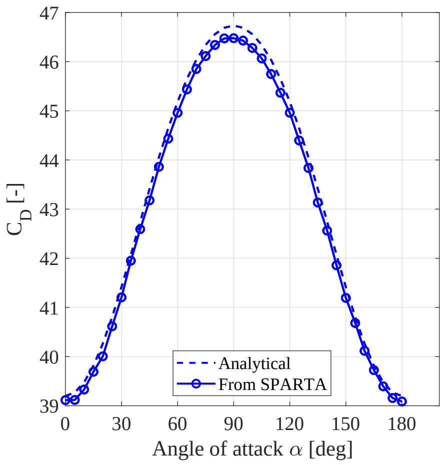

Figure 5. Comparison of C_D from SPARTA simulations and analytical calculations for cylinder

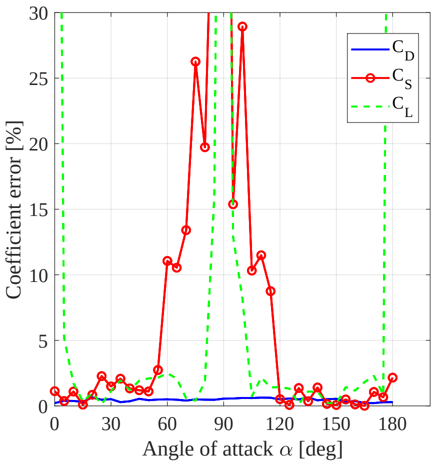

Figure 6. Percentage error in aerodynamic coefficients of the cylinder

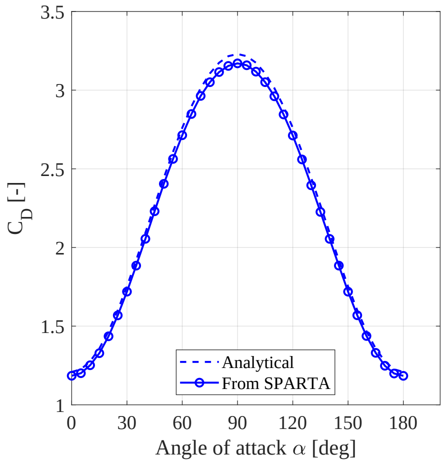

Figure 7. Comparison of C_D for flat plate from SPARTA simulations and analytical calculations

were validated across various speed ratios using the same input parameters as those used in the iteration convergence analysis. The results demonstrated strong agreement, with errors remaining below 5% at lower speed ratios and approaching 0% at higher speed ratios. This confirms the reliability of SPARTA simulations for FMF conditions. The results for the cylindrical shape are presented in Figures 5 and 6. Figure 5 shows good convergence between the C_D obtained from the SPARTA simulations and the analytical values for a speed ratio of 1. Figure 6 depicts the percentage error for the aerodynamic coefficients. The error of the drag coefficient remains nearly constant and below 1%. The lift and side-force coefficients, while mostly within the accepted range of 5% error, exhibit significant variations, reaching 100% error at angles of attack of $0°$, $90°$, and $180°$. In an ideal model, a symmetric shape, such as the cylinder or the flat plate, does not experience any lift or side force at these attitudes. However, numerical errors can cause small, non-zero forces. Therefore, although the numerical values are extremely small, the relative error spikes at 100%, as it is compared to zero. The same observations are valid for the cylinder. The results for the flat plate are presented in Figures 7 and 8. Similarly to the cylinder, Figure 7 demonstrates a strong convergence in C_D. The drag coefficient values observed for the flat plate are substantially lower than those for the cylinder. The percentage error for the flat plate is larger but remains within the accepted threshold of 5%. The lift coefficient exhibits a similar behaviour to that of the cylinder, whereas the side-force coefficient does not reach the 100% error at $\alpha = 90°$, since the flat plate experiences a non-zero side force in this configuration.

The section of the database dealing wth aerodynamic modelling is composed of one file summarising the variables described in Table 3. Along with this file, the reference surface and length are needed for proper scaling

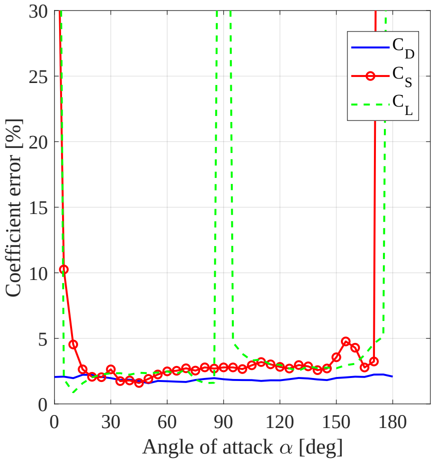

Figure 8. Percentage error in aerodynamic coefficients of the flat plate

Table 3. Variables Calculated for the Aerodynamic Model

Variable	Description
s	Speed ratio
α	Angle of attack
β	Sideslip angle
C_D, C_S, C_L	Force coefficients in $\mathcal{F}_A$
C_X, C_Y, C_Z	Force coefficients in $\mathcal{F}_B$
C_l, C_m, C_n	Moment coefficients in $\mathcal{F}_B$
T_{gas}	Gas temperature
T_w	Wall temperature
$nrho$	Gas number density
Acc_{coef}	Accommodation coefficient
$SPARTA_{steps}$	Runs per SPARTA simulation

of the coefficients; the object's geometry and reference attitude are also necessary to use the database itself.

The results of the simulations were analysed to evaluate the effects of speed ratio, angle of attack, and sideslip angle on aerodynamic behaviour.

The aerodynamic performance of the flat plate is strongly influenced by both the attitude angles and the speed ratio. These parameters determine how the flow interacts with the surfaces, affecting drag, lift, and moment coefficients. At a small angle of attack, the flow remains mostly attached to the surface, resulting in low drag and minimal lift. As the absolute value of α increases, the lift coefficient increases, reaching its maximum at $\alpha = 45°$ and its minimum at $\alpha = -45°$, before reversing its trend and attaining another peak due to flow separation and reattachment effects. On the contrary, the drag coefficient reaches its maximum at $\alpha = \pm 90°$, where the plate is oriented perpendicular to the flow, exposing the largest frontal area, thereby maximising pressure drag. The influence of the sideslip angle differs from that of the angle of attack. The maximum values of both C_D and C_L occur at $\beta = 0°$. The sideslip angle primarily modifies the flow asymmetry around the plate, without significantly increasing the projected area facing the air flow. Regarding the speed-ratio effects, at lower speed ratios, the flow remains attached to the surface for a longer time before separation occurs. This enhances both lift and drag, as a higher pressure difference develops across the surface. This phenomenon leads to higher peak values of aerodynamic coefficients compared to higher speed ratio conditions, where the reduced boundary layer attachment leads to earlier separation, diminishing lift and stabilising drag at lower values.

The aerodynamic response of the cylindrical shape differs significantly from that of the flat plate, primarily due to its curved surface. This promotes continuous flow separation and reduces sensitivity to attitude angles. Unlike the flat plate, the drag coefficient remains relatively constant across most angles of attack and sideslip angles. The most distinct aerodynamic patterns are observed at $\alpha = 0°, \pm 180°$, and $\beta = 0°$, where the drag coefficient reaches its minimum value due to a more uniform pressure distribution and reduced wake turbulence. The lift remains negligible for most angles but becomes more pronounced at moderate inclinations, particularly at $\beta = \pm 90°$ and $\alpha = \pm 40°, \pm 140°$. At these angles, an asymmetric wake structure develops, meaning that the separated flow does not symmetrically reattach behind the cylinder, leading to an uneven pressure distribution and the generation of lift [17]. Note that this effect may be more pronounced at $\alpha = \pm 45°, \pm 135°$, but these angles were not included in the current simulations. As observed for the flat plate, lower speed ratios lead to higher pressure differences across the surface, resulting in higher lift and drag coefficients. This occurs because lower relative flow velocity allows for more sustained pressure build-up before separation, enhancing aerodynamic forces.

These results have implications for space debris modelling and deorbiting strategies. The aerodynamic coefficients derived from these simulations can be incorporated into propagation models to more accurately predict the de-orbiting trajectories of space debris under varying atmospheric conditions.

3.2. Continuum Flow: Modified Newtonian

To compute the aerodynamic coefficients in the continuum flow regime, the Modified Newtonian (MN) method has been implemented. To do so, a surface mesh was first created on the surface of the objects. The mesh that was used for the cylinder is shown in Figure 9. Differently from the SPARTA implementation, the mesh used with the MN method can include both rectangular and triangular panels. The pressure coefficient of each mesh surface can be computed as [18]:

$$C_p = C_{p_{max}} \sin^2 \theta_i \tag{14}$$

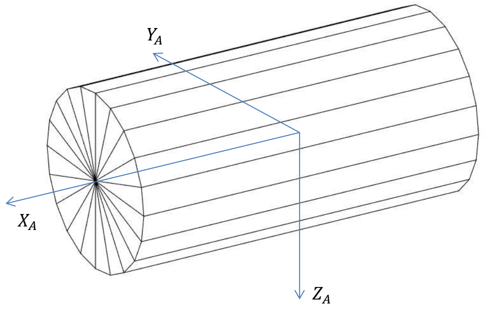

Figure 9. Cylinder mesh used in the MN method

with

$$C_{p_{max}} = \frac{2}{\gamma Ma^2}\left\{-1+\left[\frac{1-\gamma+2\gamma Ma^2}{\gamma+1}\right]\right.$$
$$\left.\left[\frac{(\gamma+1)^2 Ma^2}{4\gamma Ma^2-2(\gamma-1)}\right]^{\gamma/(\gamma-1)}\right\} \tag{15}$$

where θ_i is defined as per Equation (12), γ is the air's specific heat ratio and Ma is the Mach number of the incoming flow. The value of γ varies with altitude, but for the test cases in this work, it can be kept at 1.4. However, with test cases at higher altitudes, the decreasing value of γ should be taken into account. Note that the formulation in Equation (14) presents only the pressure term, meaning that this implementation lacks a shear component, which should be included for more accurate results.

Similarly to what was described in Subsection 3.1, a database containing the aerodynamic coefficients is created. The aerodynamic coefficients are computed using the attitude angles (α and β) and the Mach number as independent variables. The independent variables used for the continuum flow are effectively the same as those for the FMF regime, since the Mach number of the incoming stream can be expressed in terms of speed ratio as:

$$Ma = s\sqrt{\frac{2}{\gamma}} \tag{16}$$

3.3. Transition Flow

To model the aerodynamic coefficients in transition flow, two different methods were considered, out of which one is implemented in this work.

Transition flow can also be modelled with SPARTA, with a similar approach to what was described in Subsection 3.1. To adjust for the different flow regime, the number density ($nrho$) parameter needs to be adjusted. In particular, this value can be varied in the interval $(10^{-16}, 10^{-20})$ particles/m^3, depending on the object's altitude [11]. This method would provide the best estimation of the aerodynamic coefficients, with, of course, an increased computational effort due to the numerous SPARTA simulations needed. Furthermore, the introduction of an additional independent variable would greatly increase the size of the database and, as a result, the computational load to read it. The interpolation would also become more complex with the addition of one dimension, as well as more time-consuming.

The other option, which was implemented in this work, consists of creating a bridging function between the FMF and continuum flow regimes. This was applied following a formulation deduced using Space Shuttle Data [19]:

$$C_t = C_c + (C_f - C_c)\sin^2\left[\pi\frac{3+\log(Kn)}{8}\right] \tag{17}$$

where C_t, C_c, and C_f stand for the generic aerodynamic coefficient for transition, continuum, and free-molecular flow, respectively, while Kn is the Knudsen number, a parameter used to determine the current flow regime, defined as [20]:

$$Kn = \frac{\lambda}{L} \tag{18}$$

where λ is the mean molecular free path and L is the characteristic length of the flow field. Transition regime occurs when Kn is in the interval $(0.001, 10)$; rarefied flow corresponds to larger values of Kn, while continuum regime is characterized by smaller Knudsen numbers.

4. EXAMPLE APPLICATIONS

This section presents the results in which the space debris database described in the previous section is used for the propagation of the two objects of interest, namely the cylinder and the flat plate.

Both objects are placed at an altitude of about 180 km with the following initial state, expressed in $\mathcal{F}_I$ as:

$$\mathbf{r}_I = \begin{pmatrix}5.636\cdot10^3 & -3.362\cdot10^3 & 5.872\end{pmatrix}^T \text{ km} \tag{19}$$

$$\mathbf{v}_I = \begin{pmatrix}3.317 & 5.634 & 4.221\end{pmatrix}^T \text{ km/s} \tag{20}$$

with zero components of the angular velocity. The simulations are carried out in the environment described in Section 2 until the object reaches a termination altitude of 120 km, where the re-entry point is defined. For the aerodynamic modelling, three different cases are implemented in the simulations: i) a 6 degrees-of-freedom (dof) simulation with aerodynamic force and moment coefficients estimated at each time interval from the database (finite-body model); ii) a 3-dof simulation that uses the finite-body model for the aerodynamics; iii) a 3-dof simulation using a cannonball drag model. The 6-dof simulation is the most accurate out of the three options but also the most computationally expensive. Therefore, a comparison between these aerodynamic models is performed, with the 6-dof simulation as a benchmark, to determine whether the other options would provide suitable results with less computational effort.

Table 4. Re-entry conditions for the cylinder

Parameter	Case i)	Case ii)	Case iii)
t (s)	1645	1634	2020
τ (deg)	-110.8	-111.5	-85.1
δ (deg)	29.9	30.1	20.8
v (km/s)	7.841	7.834	7.856
γ (deg)	-0.248	-0.258	0.008
χ (deg)	104.9	104.5	117.5

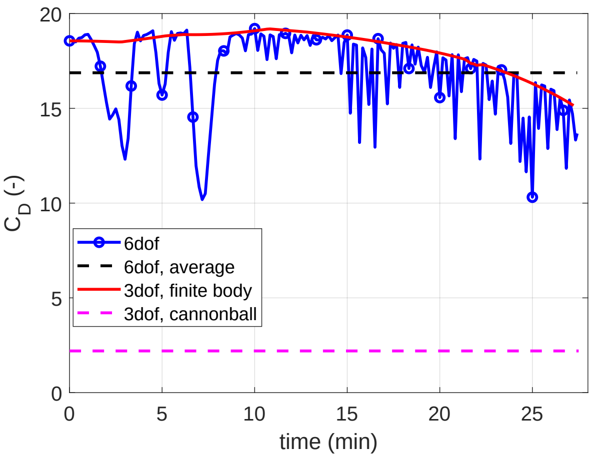

Figure 10. Drag coefficients of the different cases for the cylinder over the simulation time

First, the nominal simulations for the cylindrical object were performed with the three aerodynamic models described above. The results of these simulations are shown in Table 4, where the final conditions are expressed in terms of final epoch (t), longitude (τ), latitude (δ), velocity norm (v, expressed in $\mathcal{F}_I$), flight path angle (γ), and heading angle (χ). Based on the final longitude and latitude, the distance from the benchmark re-entry point is calculated, resulting in 86 km for case ii), i.e., 3-dof finite-body, and 2746 km for case iii), i.e., cannonball.

To understand the reasons behind the differences in these three cases, Figure 10 shows the evolution of the drag coefficients over the simulation time. Concerning the cannonball model, it is evident how it is extremely disadvantaged due to the much lower value of the drag coefficient. For this reason, a fourth case, which will be referred to as case iv), is implemented: a 3-dof simulation that uses the cannonball model, where the drag coefficient is the average value from case i), shown in Figure 10 as the black dashed line. Case iii) will not be discussed further, and case iv) will be the new cannonball model from now on, with a constant drag coefficient of $C_D = 16.88$. The re-entry point for this fourth case is much closer to the benchmark one, with a final distance of about 34 km.

When comparing finite-body models, the drag coefficients follow the same trend overall, although the 6-dof simulation presents frequent dips, suggesting a less intense effect of drag over time, which would explain the longer flight time and the difference in final position. To fully understand the effect of these differences, Figure 11 shows the integral of the drag and lift forces over the simulation time. As expected, the integral of drag is slightly higher for case ii) than for case i). Also, the effect of drag in case iv) is closer to the benchmark, which is explained by the new cannonball model that is tailored to the 6-dof simulation. As shown in Figure 11, lift might also play a role in the simulation, although its magnitude is negligible compared to drag. Nevertheless, the zero lift that characterises the cannonball model is closer to the lift effect in the 6-dof simulation, while case ii) presents a positive lift effect over the first part of the simulation.

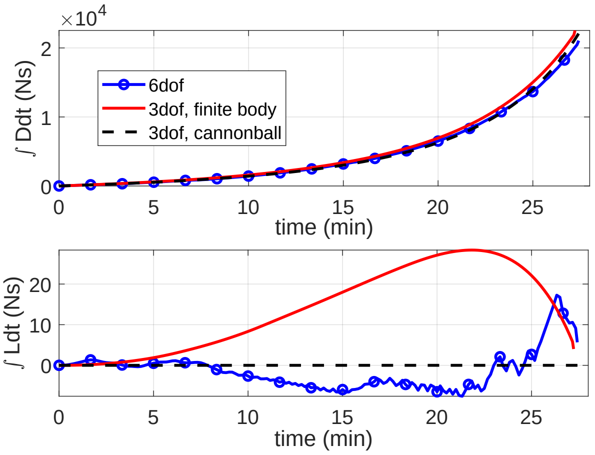

Figure 11. Integral of drag (top) and lift (bottom) force over time during the cylinder's orbital decay

Table 5. Impact conditions for the cylinder

Parameter	Case i)	Case ii)	Case iv)
t (s)	889	862	947
τ (deg)	-65.2	-67.3	-72.0
δ (deg)	9.1	10.5	13.5
v (m/s)	472.3	470.3	455.5
d (km)	N/A	281.4	887.7

Although the final distances between re-entry points might seem small, it should be taken into account that the simulation times are quite restricted, meaning that, if a longer simulation were to be performed, the final distance would be larger. Furthermore, the present simulations stop at 120 km: analysing the impact location would provide additional insights on how the distance from the benchmark evolves after the re-entry point.

To do so, a second set of simulations was performed, using the re-entry point as initial state and 20 km as termination altitude. The results of the impact analysis are shown in Table 5, where t is the flight time of only the impact trajectory. The distance from the benchmark impact point is also shown as d. In this second propaga-

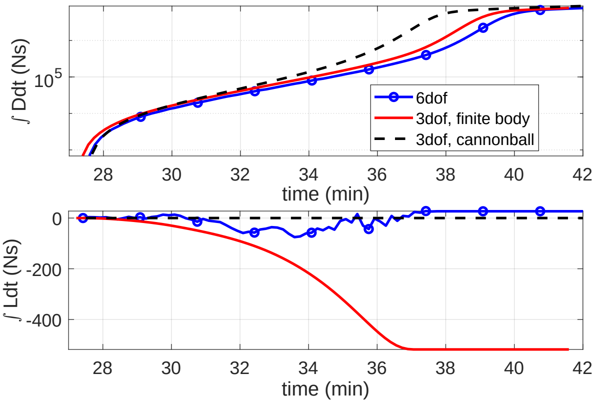

Figure 12. Integral of drag (top) and lift (bottom) force over time between the cylinder's re-entry and impact points

Table 6. Distribution of implemented uncertainties

Parameter	PDF family	μ	σ
$\mathbf{r}$ (m)	Normal	$[0, 0, 0]$	$[10^3, 10^3, 10^3]$
$\mathbf{v}$ (m/s)	Normal	$[0, 0, 0]$	$[10, 10, 10]$
$\boldsymbol{\omega}$ (deg/s)	Uniform	$[0, 0, 0]$	$[1, 1, 1]$
$\ln(\rho)$ (kg m^{-3})	Normal	0	20%
m (kg)	Uniform	0	50
$\mathbf{I}$ (kg m^2)	Uniform	$[0, 0, 0]$	$[10\%, 10\%, 10\%]$
C_D, C_S, C_L	Uniform	$[0, 0, 0]$	$[10\%, 10\%, 10\%]$
C_l, C_m, C_n	Uniform	$[0, 0, 0]$	$[15\%, 15\%, 15\%]$

tion, case iv) deviates much more from the benchmark impact point, while case ii) shows closer results. Similarly to the orbital decay analysis, the integral of drag and lift over time is plotted in Figure 12. This time, case ii) shows an important contribution of negative lift, explaining its flight time being the lowest. For what concerns drag, the final value of its integral over time appears to be the same among the three cases, but case iv) shows a peak in drag much earlier than the rest. This is due to the value of the cannonball drag coefficient being now much higher compared to the benchmark one, which was, on average, halved compared to the orbital decay simulation. This highlights the main limitation of using a cannonball model tailored to the benchmark simulation: the average value from the 6-dof simulation might not be applicable for different situations, such as the impact trajectory, or even when the initial state is perturbed.

As mentioned in Section 2, there are different sources of uncertainties in the upper atmosphere. To analyse the effects of the perturbations introduced by these uncertainties, Monte Carlo simulations were carried out, with a particular interest in how these affect the re-entry point when considering the three different aerodynamic models. Table 6 shows the perturbations applied to the simulations in terms of probability density function family, mean, and standard deviation. The parameters impacted by these perturbations are the initial position $\mathbf{r}$, initial velocity $\mathbf{v}$, initial angular velocity $\boldsymbol{\omega}$, atmospheric density ρ, mass m, inertia tensor $\mathbf{I}$, and aerodynamic force and moment coefficients. The perturbations on aerodynamic moment coefficients are, of course, relevant only for the 6-dof simulation.

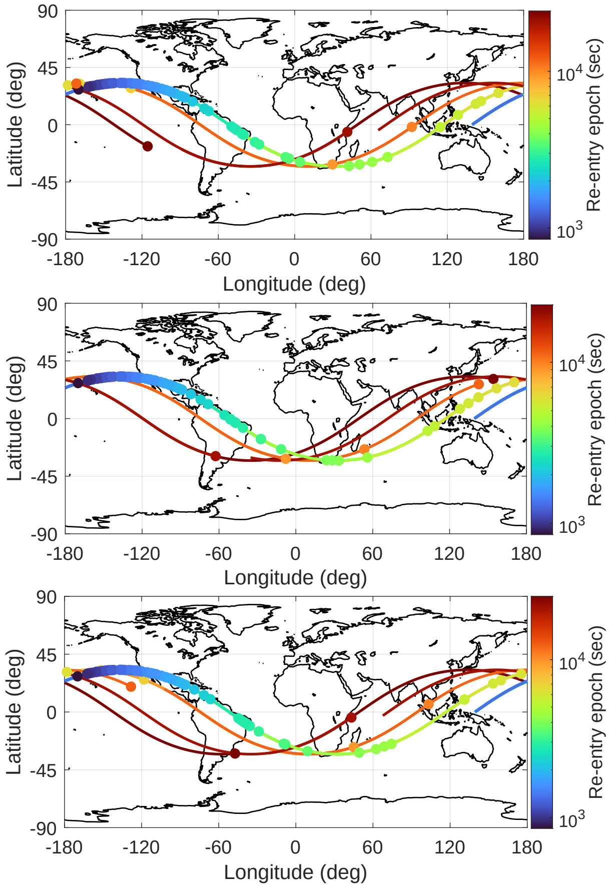

Figure 13. Re-entry location and time of the Monte Carlo analysis for different aerodynamic modelling and the cylindrical object

A total of 100 simulations were performed for each of the aerodynamic models: this batch is quite small but was limited by the long runtimes that incur when propagating with 6 degrees of freedom. Figure 13 shows the final position on the Earth's map for all of these simulations. In particular, case i) is the subplot at the top, case ii) in the middle, and case iv) at the bottom. The different re-entry points are shown together with different colours representing their respective re-entry epochs, and their ground tracks are also plotted. For longer simulations that complete multiple orbits before re-entry, only the last orbit is shown as a ground track. The colour of the re-entry points can also be used to distinguish, along the three cases, simulations with the same perturbations. From Figure 13, it is evident that the cannonball model performs better than the 3-dof finite-body model at approximating the final position of the 6-dof simulations. Figure 14 shows the relation between the final distance

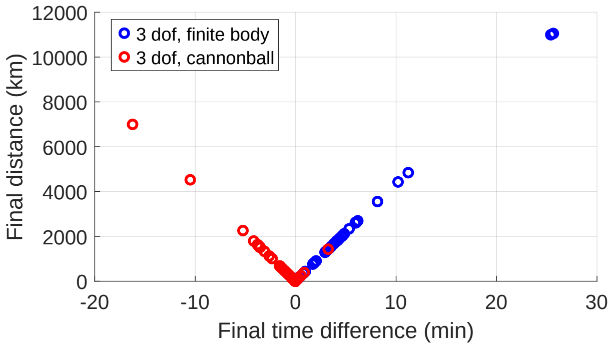

Figure 14. Relation between final distance and final time difference between Monte Carlo simulations

and time difference from the benchmark re-entry points. Note that these differences are not computed by comparing the Monte Carlo re-entry points to the nominal benchmark re-entry point; on the contrary, the comparison is made between simulations with the same perturbations. As previously concluded, the results from Figure 14 show that the cannonball model is able to better predict the benchmark re-entry position. A tendency of the cannonball model to impact later than in the 6-dof case is also observed, while the results in case ii) generally reach the termination altitude earlier. As suspected, there is a linear dependency between the final position and time differences. The nominal simulation at hand reaches the termination altitude immediately, without performing multiple orbits. When the nominal conditions are perturbed, the object sometimes travels on several orbits before reaching the re-entry point, and this is when the higher final distance and time difference are observed. This means that, for a large number of applications, where the object travels over a few orbits, the final distances are going to be more pronounced, likely in the order of thousands of kilometres.

For what concerns the flat plate, the nominal simulations were performed over cases i), ii), and iv). This example presents interesting results compared to the previous test case due to the much smaller dimensions and mass of the plate. Now, case iii) is skipped completely, and the cannonball coefficient used in case iv) is $C_D = 0.0495$. This value is much smaller than that of the cylinder, but this is due to the low values of the angle of attack along the 6-dof simulation. The re-entry conditions for the three aerodynamic models are shown in Table 7. One of the most striking results is the much longer flight time for case ii), where the object completes an additional orbit before reaching 120 km. Figure 15 shows the evolution of the drag coefficient (top) and the drag integral (bottom) over time; note that the full simulation time is not shown for case ii) to ease the reading.

The 3-dof finite-body case shows an overall lower drag effect, which explains why it did not reach the termination altitude as soon as the other two cases did. It is also interesting how the drag effect for case iv) ended up being much larger than that for the benchmark, and how the

Table 7. Re-entry conditions for the flat plate

Parameter	Case i)	Case ii)	Case iv)
t (s)	1950	6990	1938
τ (deg)	-89.7	-126.0	-90.5
δ (deg)	$2.282 \cdot 10^1$	$2.800 \cdot 10^1$	$2.315 \cdot 10^1$
γ (deg)	-0.012	-0.099	-0.034
χ (deg)	115.6	108.8	115.3
d (km)	N/A	3684	85.1

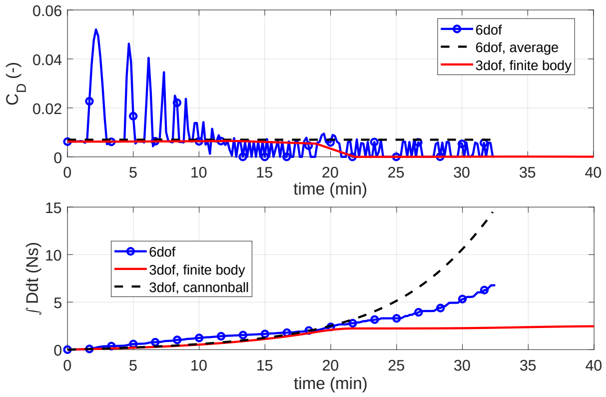

Figure 15. Drag coefficient (top) and drag integral over the simulation time (bottom) for the flat plate

distance in re-entry points is now more pronounced when compared to the cylinder test case. This is because, over the simulation, the benchmark drag coefficient presents an oscillatory behaviour, with peaks that are much higher during the first ten minutes of the simulation than in the last part. The average value seems to be highly influenced by the behaviour at the beginning of the simulation. This causes the cannonball drag effect to be slightly lower at the beginning but much higher in the last leg of the trajectory. Compared to the cylinder case, the trend of the 6-dof simulation drag coefficient shows more variability. In a way, this result is similar to what was observed with the impact analysis for the cylinder.

5. CONCLUSIONS

In this paper, a method to obtain a database that includes improved aerodynamic modelling of space debris objects in different flow regimes was presented. For rarefied flow, the Stochastic Parallel Rarefied-gas Time-accurate Analyzer (SPARTA) software was employed: due to its complexity, a thorough evaluation of the input parameters was made in order to balance result accuracy and computational runtime. For continuum flow, the Modified Newtonian method was employed, and a bridging function was built for transitional flow.

The database was then developed for two objects of simple shapes, namely a flat plate and a cylinder, and employed in an orbital decay simulation, plus a re-entry simulation for the cylinder. Three different aerodynamic models were tested: i) a 6 degrees of freedom (dof) simulation that uses the aerodynamic coefficients from the database; ii) a 3-dof simulation that uses the aerodynamic coefficients from the database; iii) a cannonball drag model with $C_D = 2.2$. Due to its extremely poor performance, case iii) was eventually discarded. Thus, a fourth case was introduced: iv) a cannonball simulation with the average drag coefficient of the 6-dof simulation as C_D.

For the cylinder test case, the nominal simulations were first analysed, with case iv) proving quite promising, while the re-entry points for both cases were less than 100 km distant from the benchmark result. However, when the simulation was extended to reach the impact point, the final distance from the 6-dof simulation had increased greatly. Furthermore, the performance of case iv) was much worse, with the final distance nearing a thousand kilometres. This was mainly due to the choice of cannonball drag coefficient, which was tailored for the orbital decay but was not suitable when the simulation continued beyond the re-entry point. Subsequently, a Monte Carlo analysis was performed for the orbital decay. The cylinder's state and characteristics were perturbed, as well as the atmospheric density, so as to model the uncertainties over these parameters. Similarly to previous results, case iv) proved to perform much better than case ii), although the distances from the baseline results in simulations with longer flight times were still quite high. When considering a nominal simulation that orbits multiple times before reaching the termination altitude, the final distance from the 6-dof simulation can be predicted to be in the order of thousands of kilometres for both cases.

For the flat plate, the nominal simulations were performed. This case proved quite interesting, as the case ii) simulation performed an additional orbit before reaching the termination altitude. Once again, the adjusted cannonball model performed well, but the final distance from the baseline re-entry point was larger than the one for the cylinder, proving that not only the average value of C_D is relevant, but its behaviour over the simulation should also be taken into account.

In conclusion, while a cannonball model can provide an approximation of a 6-dof simulation, only with C_D tailored accordingly, it is not a good enough model. Furthermore, using an averaged drag coefficient based on the 6-dof simulation defeats the purpose of using a less computationally expensive model, as the more CPU intense one still needs to be employed. A 3-dof simulation that uses the database coefficients also proved to be not good enough, generally performing worse than the adjusted cannonball model. The analyses performed in this paper suggest that a 6-dof simulation is the only acceptable solution in terms of accuracy and that the aerodynamic modelling should comprise a database similar to the one introduced in this work. However, the extent of these conclusions is constrained by the number of objects simulated and their simple geometries. Therefore, the database should be expanded with objects that present more complex geometries so to fully take advantage of the SPARTA software, and simulations similar to those presented in this work should be performed to understand the effects of different aerodynamic modelling in different case scenarios. Furthermore, improvements still need to be made in the modelling, accounting for solar and geomagnetic activity in longer simulation cases and implementing a more accurate atmospheric model. Finally, the 6-dof simulation is stated to be very computationally expensive, but some improvements could be studied to reduce the CPU runtime of the algorithm currently employed.

REFERENCES

1. ESA Space Debris Office, (2024). ESA's annual space environment report, Ref. GEN-DB-LOG-00288-OPS-SD, Issue 8.
2. Headstream, J.A. and Manis, A., (2024). "Goldstone Radar Measurements of the Orbital Debris Environment: 2022," NASA Orbital Debris Quarterly News, Vol. 28, No. 1.
3. March, G. (2020), "Consistent Thermosphere Density and Wind Data from Satellite Observations", PhD thesis, Delft University of Technology.
4. Hoogendoorn, R., Mooij, E., & Geul, J. (2018), "Uncertainty propagation for statistical impact prediction of space debris", *Advances in Space Research*, Vol. 61, No .1, pp.167-181.
5. Bruinsma, S., Dudok de Wit, T., Fuller-Rowell, T., Garcia-Sage, K., Mehta, P., Schiemenz, F., Shprits, Y.Y., Vasile, R. Yue, J., & Elvidge, S., (2023). "Thermosphere and satellite drag", *Advances in Space Research*. https://doi.org/10.1016/j.asr.2023.05.011
6. Picone, J.M., Hedin, A.E., Drob, D.P., & Aikin, A.C. (2002), "NRLMSISE-00 empirical model of the atmosphere: Statistical comparisons and scientific issues", *Journal of Geophysical Research: Space Physics*, Vol. 107, No. A12, SIA-15.
7. Mehta, P.M., Paul, S.N., Crisp, N.H., Sheridan, P.L., Siemes, C., March, G., & Bruinsma, S., (2023). "Satellite drag coefficient modeling for thermosphere science and mission operations", *Advances in Space Research*, Vol. 72, No. 12, pp. 5443-5459. https://doi.org/10.1016/j.asr.2022.05.064
8. Fang, T.W., Kubaryk, A., Goldstein, D., Li, Z., Fuller-Rowell, T., Millward, G., Singer, H.J., Steenburgh, R., Westerman, S., & Babcock, E., (2022). "Space Weather Environment During the SpaceX Starlink Satellite Loss in February 2022", *Space Weather*, Vol. 20. No. 11, e2022SW003193. https://doi.org/10.1029/2022SW003193
9. Ronse, A.L.A.B., & Mooij, E., (2014). "Statistical impact prediction of decaying object", *Journal of Spacecraft and Rockets*, Vol. 51, No. 6, pp. 1797-1810.

10. Hładczuk, N. (2023), “SPARTA DSMC Simulator Manual”, Delft University of Technology, Internal report.
11. Peña Arambarri, L.M. (2023). “Orbital decay of objects in a low Earth orbit”, MSc thesis, Delft University of Technology.
12. Doornbos, E., (2012). *Thermospheric Density and Wind Determination from Satellite Dynamics*, Springer Science and Business Media. https://doi.org/10.1007/978-3-642-25129-0.
13. Mehta, W., McLaughlin, R., Koller, J., (2014). “Comparing physical drag coefficients computed using different gas surface interaction models”, *Journal of Spacecraft and Rockets*, Vol. 51, No. 3, pp. 873-883. https://doi.org/10.2514/1.A32566.
14. Toonen, L.M., (2021). “Horizontal wind influence on satellite aerodynamics at the edge of space”, MSc thesis, Delft University of Technology.
15. Sentman, L.H. (1961), “Free Molecule Flow Theory and Its Application to the Determination of Aerodynamic Forces”, Lockheed Missiles & Space Company, Technical Report LMSC-448514.
16. Hart, K.A., Dutta, S., Simonis, K., Steinfeldt, B.A., & Braun, R. D. (2014), “Analytically-derived aerodynamic force and moment coefficients of resident space objects in free-molecular flow”, in *AIAA Atmospheric Flight Mechanics Conference*, pp. 0728. DOI: https://doi.org/10.2514/6.2014-0728.
17. Anderson, J.D., Jr. and Cadou, C.P., (2024). *Fundamentals of Aerodynamics*, McGraw-Hill, ed. 7, ISBN 978-1-266-07644-2.
18. Mooij, E., (2024). *Re-entry systems*, Springer Nature.
19. Blanchard, R.C., & Buck, G.M., (1986). “Rarefied-Flow Aerodynamics and Thermosphere Structure for Shuttle Flight Measurements.”, *Journal of Spacecraft*, Vol.23, No.1.
20. Regan, F.J., & Anandakrishnan, S.M., (1993). *Dynamics of Atmospheric Re-entry*, AIAA.